Tensile Deformation Behavior and Phase Transformation in the Weld Coarse-Grained Heat-Affected Zone of Metastable High-Nitrogen Fe-18Cr-10Mn-N Stainless Steel

JOONOH MOON, TAE-HO LEE, SEONG-JUN PARK, JAE-IL JANG, MIN-HO JANG, HEON-YOUNG HA, and BYOUNGCHUL HWANG

The tensile deformation behavior and phase transformation in the weld coarse-grained heat-affected zone (CGHAZ) of a metastable high-nitrogen austenitic stainless steel was explored through tensile tests, nanoindentation experiments, and transmission electron microscopy analysis. True stress–strain response during tensile test was found to be seriously affected by δ-ferrite fraction, which depends on peak temperature of the CGHAZs. The strain-induced martensitic transformation (SIMT) occurred in base steel, whereas the SIMT disappeared and deformation twinning occurred predominantly in the CGHAZs. The relationship among true stress–strain response, nanoindentation hardness, and deformed microstructures was carefully investigated and discussed in terms of changes of stacking fault energy.

DOI: 10.1007/s11661-013-1682-2

I. INTRODUCTION

In recent years, high-N, Ni-free austenitic stainless steels (HNS) have been developed aiming to replace the conventional Cr-Ni austenitic stainless steels because Ni increases the material cost and causes an environment problems.[1] This replacement is likely because N is a strong austenite-stabilizing element and thus makes it possible to retain austenite phase without the addition of Ni. Cr addition in stainless steel forms δ-ferrite during solidification, and this inhibits N solution in HNS because N solubility in δ-ferrite is very limited. Therefore, HNS is usually manufactured using a pressurized vacuum-induction melting furnace to shorten δ-ferrite solidification range.

HNS has attracted considerable interest on account of its good combination of mechanical properties and corrosion resistance[2]: N is well known to enhance yield strength without a significant loss of ductility and toughness. Irvine *et al.*[3] examined the solid-solution strengthening effects of alloying elements in austenitic stainless steels and reported that interstitial elements such as C and N are the most effective to increase 0.2 pct proof yield strength. N has been also reported to improve the pitting corrosion resistance by producing more protective passive film.[4]

In addition, it has been accepted that N increases the stacking fault energy (SFE) of austenite and thus has a significant effect on plastic deformation behavior.[5,6] Lee *et al.*[6] reported that deformation-induced microstructural change of HNS can be classified into three groups: (1) strain-induced martensite transformation (SIMT) in low SFE alloys, (2) deformation twinning (DT) in high-SFE alloys, and (3) mixture of SIMT and DT in intermediate SFE alloys. Lee *et al.*[2] also suggested that the critical N content for SIMT in Fe-18Cr-10Mn-N alloy is around 0.5 wt pct, from analyzing true stress–true strain curves. The SIMT in HNS is a very important phenomenon to determine the mechanical properties of the material, and thus much research has been performed on the relationship among austenite stability, microstructure, and mechanical behavior.[2,7,8] On the other hand, the excellent mechanical properties of HNS can be upset during the welding process because the welding thermal cycle can significantly change the microstructures and in turn the mechanical properties. In particular, the mechanical behavior of the weld coarse-grained heat-affected zones (CGHAZs) should be carefully examined because the CGHAZs are expected to show relatively poor mechanical properties due to their coarse grain size and formation of local brittle zone. Nevertheless, it is somewhat surprising that few studies on the weld characteristics of HNS are available in the literature.[1,9]

With all this in mind, in this article we evaluate the plastic deformation and phase transformation behavior in the weld CGHAZ of a HNS Fe-18Cr-10Mn-N alloy. The simulated CGHAZ samples were prepared by Gleeble simulator (Dynamic Systems Inc., Poestenkill,

JOONOH MOON, SEONG-JUN PARK, and HEON-YOUNG HA, Senior Researchers and TAE-HO LEE, Principal Researcher, are with the Ferrous Alloy Department, Advanced Metallic Materials Division, Korea Institute of Materials Science, Changwon, Gyeongnam 642-831, Republic of Korea. Contact e-mail: mjo99@kims.re.kr. JAE-IL JANG, Professor, is with the Division of Material Science and Engineering, Hanyang University, Seoul 133-791, Republic of Korea. MIN-HO JANG, Researcher, is with the Department of Materials Science and Engineering, University of Science and Technology, Yuseong-ku, Daejeon 305-350, Republic of Korea. BYOUNGCHUL HWANG, Assistant Professor, is with the Department of Materials Science and Engineering, Seoul National University of Science and Technology, 232 Gongneung-ro, Nowon-gu, Seoul 139-743, Republic of Korea.

Manuscript submitted August 20, 2012.
Article published online March 13, 2013

NY), and the distribution of alloying elements were analyzed using electron probe microanalysis (EPMA). The deformation behavior of the CGHAZ samples was evaluated using tensile tests and nanoindentation experiments, and was compared with that of base steel. Finally, the deformed microstructures of both base steel and CGHAZs were analyzed using transmission electron microscopy (TEM).

II. EXPERIMENTAL PROCEDURES

The chemical composition of HNS used in this study was Fe-17.96Cr-9.74Mn-0.03Si-0.33N-0.03C (wt pct), and balance Fe. High Mn contents (of around 10 wt pct) were selected to achieve fully austenitic microstructure without Ni addition and to increase N solubility. Ingot was fabricated using a commercial pressurized vacuum-induction melting furnace (VIM 4 III-P; ALD Vacuum Technologies, Hanau, Germany) under nitrogen partial pressure of 1 bar. After homogenization at 1523 K (1250 °C) for 2 hours, the ingot was first hot rolled into sheet of 4 mm in thickness and then air cooled to room temperature. To make fully austenite microstructure, the specimen was reheated to 1273 K (1000 °C) for 1 hour and then quenched into water. Figure 1 exhibits results of Thermo-Calc (Thermo-Calc, Stockholm, Sweden) calculation: (1) the phase diagrams and (2) the changes in volume fraction of austenite and δ-ferrite as a function of temperature. As shown in Figure 1, only austenite is stable at 1273 K (1000 °C). The CGHAZs were simulated using Gleeble simulator (Gleeble-3500, Dynamic Systems, Inc.) according to a thermal cycle scheme illustrated in Figure 2. The thermal cycle in Figure 2 was determined based on Rosenthal's heat-flow equation for simulating the welding condition of 30 kJ/cm heat input.[10] As seen in Figure 2, we prepared three CGHAZs by applying different peak temperatures (1473 K, 1573 K, and 1623 K [1200 °C, 1300 °C, and 1350 °C]). Microstructural observations of base metal and CGHAZs were carried out with an optical microscope using the samples that were electrolytically etched in a mixed solution of 100 mL distilled water and 10 g oxalic acid. The phases in tested alloys were identified by X-ray diffraction (XRD; D/Max 2500; Rigaku Corporation, Tokyo, Japan) using Cu K_α radiation with graphite monochromator on the mechanically polished flat surface. True stress–strain relation of all specimens (ASTM E8M) was obtained through a tensile test machine (Instron 5882, Instron Corporation, Canton, MA) at ambient temperature at a nominal strain rate of 1.33×10^{-3} seconds^{-3}. EPMA (JXA-8500F; JEOL Ltd., Tokyo, Japan) was carried out to examine the partitioning of alloying elements with the formation of δ-ferrite. Nanoindentation experiments were performed at a peak load of 10 mN using a Nanoindenter-XP (Agilent Technologies, Santa Clara, CA) equipped with a Berkovich indenter. Finally, thin foils for TEM were prepared in a twin-jet electrolytic polishing using a mixed solution of 10 pct perchloric acid and 90 pct methanol, and they were observed in a TEM (JEM2100F; JEOL Ltd.) at 200 kV for examining the deformed microstructures of base steel and CGHAZs.

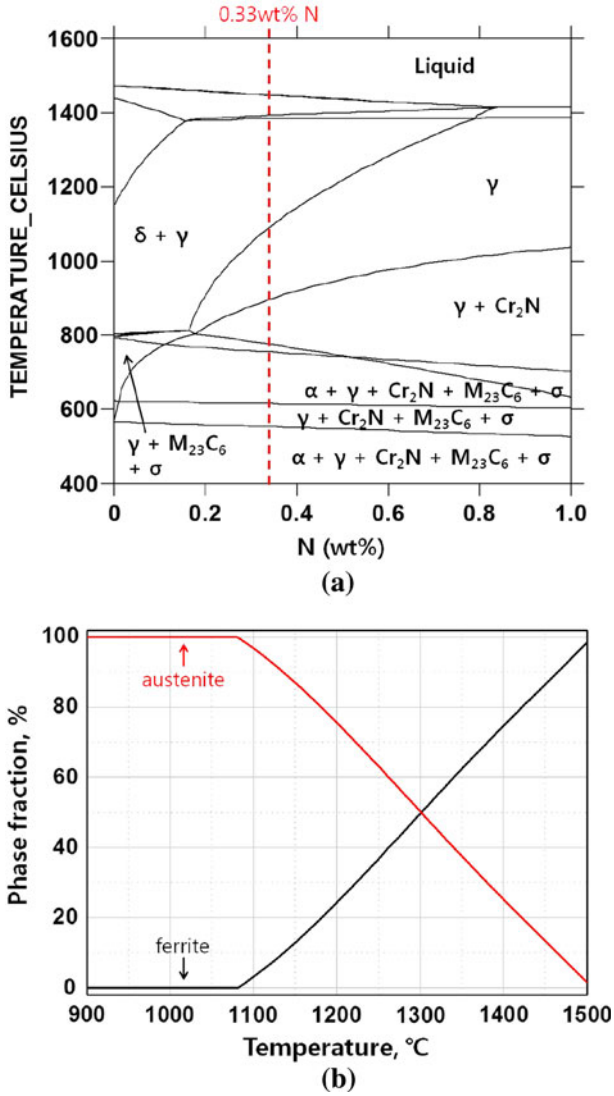

Fig. 1—Calculated phase diagram for experimental alloy: (*a*) isopleths diagram and (*b*) volume fraction of ferrite and austenite with increasing temperature.

III. RESULTS AND DISCUSSION

A. *Microstructure Before Deformation*

From the Thermo-Calc calculation in Figure 1, one may expect that the volume fraction of δ-ferrite increases with increasing peak temperature in the CGHAZ. The actual volume fraction of δ-ferrite was experimentally measured by an image analyzer using optical micrographs, and Table I lists the measurement results together with calculated ones. The trend of experimental results is in an agreement with that of calculated results; the volume fraction of δ-ferrite clearly increases with peak temperature. The measured fraction of each CGHAZ is smaller than the calculated fraction perhaps because the phase fraction did not reach the equilibrium states during the fast heating and cooling process in Figure 2. Figure 3 shows representative optical micrographs for the base steel and simulated CGHAZs. As expected, the base steel consists of only

austenite. The δ-ferrite is observed in the CGHAZs and its fraction increases with increasing peak temperature as shown in Figures 3(b) through (d) and Table I. The results of XRD analysis in Figure 4 show that only two phases of austenite and ferrite existed in the CGHAZs, supporting that newly formed phases found in the CGHAZ of Figure 3 are δ-ferrites. Note that the secondary phases like Cr_2N particle, $M_{23}C_6$ particle, and σ phase in Figure 1(a) were not observed in the CGHAZs. This may be associated with the cooling time; *i.e.*, while previous work[11] reported that the secondary phases require enough times for precipitation (for example, longer than 1000 seconds at 1123 K [850 °C] for grain boundary Cr_2N), the fast cooling rate adopted in this work did not allow sufficient time for the nucleations of the secondary phases.

B. *True Stress–Strain Response*

Figure 5 shows the true stress–strain curves of the base steel and CGHAZs obtained from tensile tests. In Figure 5, the stress–strain curves for base steel and CGHAZ 1 (with peak temperature of 1473 K [1200 °C]) are sigmoidal shaped and exhibit a transition point of strain (that is over 0.15), which is known to be an indicator of the onset of SIMT.[2,12] In the previous work,[2] Lee *et al.* determined the this transition point using modified Ludwik equation ($\sigma = K_1\varepsilon^{n_1} + \Delta$, where, $\Delta = \exp(k_2 + n_2\varepsilon)$), which is known to be a suitable model for describing σ–ε behavior of face-centered cubic materials that do not show SIMT. That is, the stress–strain curves were empirically fitted into the modified Ludwik equation and then the transition points of stress–strain curves for base steel and CGHAZ 1 were determined as a point which the experimental stress–strain curves deviated from the modified Ludwik relation. This SIMT behavior is also strong evidence for the fact that the stability of austenite in base steel and CGHAZ 1 is relatively low (metastable). Interestingly, the SIMT was retarded in CGHAZ 1 vis-à-vis base metal and disappeared in CGHAZ 2 and 3, having a higher peak temperature of 1573 K and 1623 K (1300 °C and 1350 °C). This may be due to the fact that the austenite stability and the SFE can be significantly influenced by the formation of δ-ferrite in the CGHAZ. Equilibrium solute concentrations in austenite region of the tested steel were calculated using Thermo-Calc and the calculation results are described as function of temperature in Figure 6 where the concentration of austenite-stabilizing elements, such as Mn, C, and N, in austenite phase increases with increasing temperature at ferrite-austenite ($\delta+\gamma$) region. The increase in the fraction of δ–ferrite with the temperature at the $\delta+\gamma$ region (see Figure 1(b)) implies that, in nature, more austenite-stabilizing elements should be concentrated at the austenite region with increasing temperature, as shown in Figure 6. The calculation result in Figure 6 was confirmed experimentally by EPMA analysis in Figure 7. In Figure 7, Cr is enriched in ferrite phase as a ferrite stabilizer, while Mn and N are enriched in austenite phase as austenite stabilizers. Although C should be concentrated in the austenite phase, the partitioning of C was not detected clearly by EPMA. This is presumably related to the resolution of EPMA used in this research; that is, the experimental alloy in this study contains very low carbon contents (0.03 wt pct), and this is the C range that EPMA is not able to analyze reliably. This enrichment of alloying elements in austenite inhibits SIMT and promotes DT by increasing the SFE together with austenite stability. In the Section III–D, the SFE of our samples is quantitatively estimated, and the change of deformation according to increase in SFE is discussed in detail.

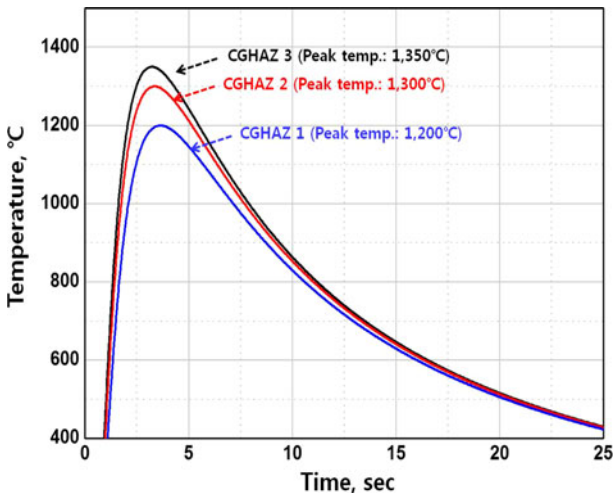

Fig. 2—Calculated thermal cycle in the weld heat-affected zone by Rosenthal equation.[10]

C. *Nanoindentation Hardness*

Next, we estimated the nanohardness of austenite phase in each sample through nanoindentation experiments that are known to be useful to evaluate the mechanical property of single phase in polycrystalline metal.[13] Figure 8 shows representative nanoindentation load (P)-displacement (h) curves of austenite phase in each steel. Selection of the curve for austenite phase

Table I. Volume Fraction of δ-Ferrite and Austenite in the Weld CGHAZs

		The Ratio of Austenite and δ-Ferrite, $\gamma : \delta$	
	Peak Temperature [K (°C)]	Calculated	Measured
CGHAZ 1	1473 (1200)	76 : 24	82 : 18
CGHAZ 2	1573 (1300)	50 : 50	64 : 36
CGHAZ 3	1623 (1350)	38 : 62	59 : 41

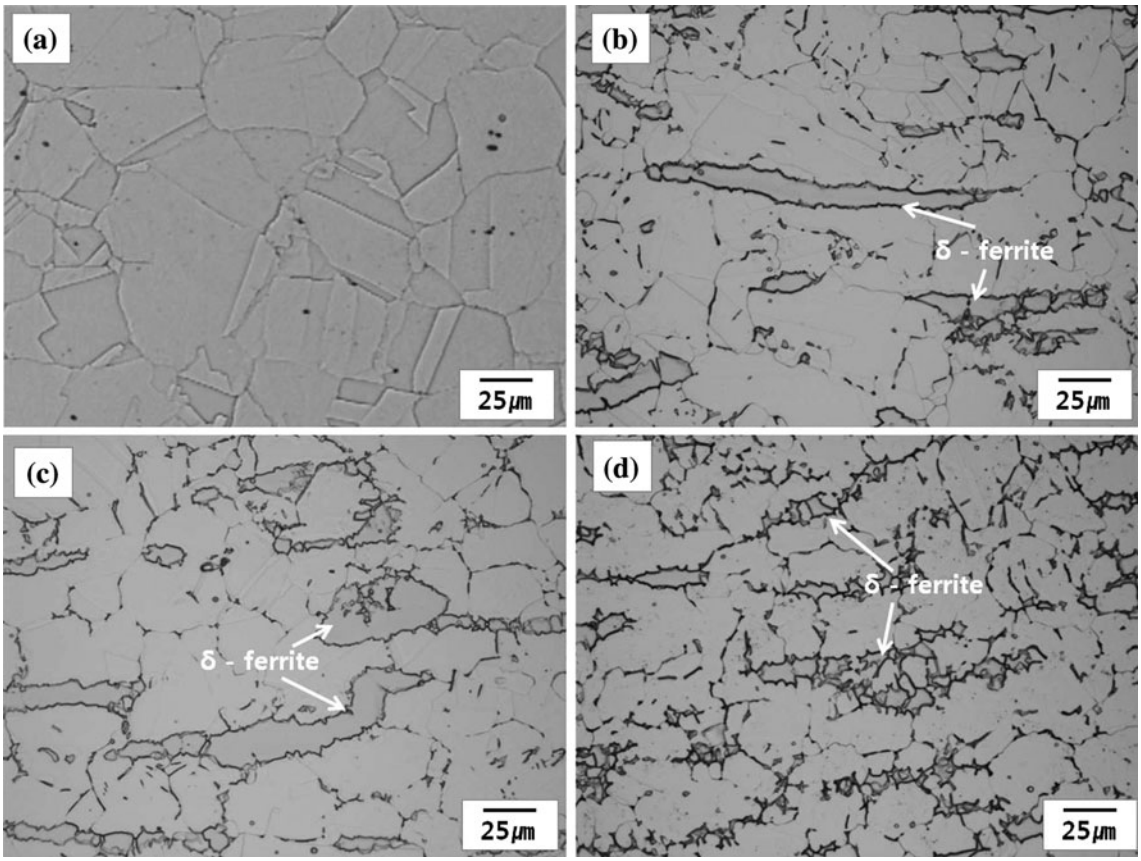

Fig. 3—Microstructures in the base steel and simulated CGHAZs: (*a*) base metal, (*b*) CGHAZ 1 with 1473 K (1200 °C) peak temperature, (*c*) CGHAZ 2 with 1573 K (1300 °C) peak temperature, and (*d*) CGHAZ 3 with 1623 K (1350 °C) peak temperature, respectively.

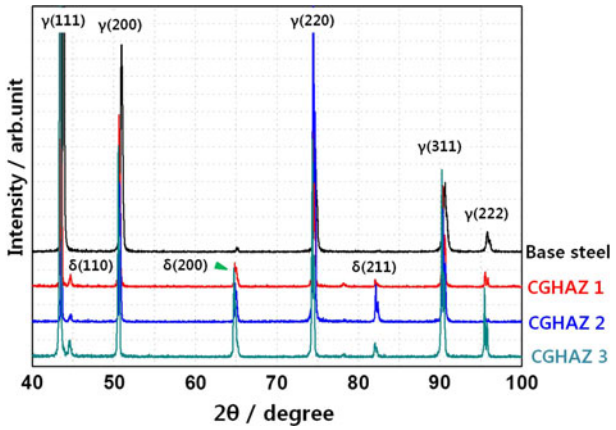

Fig. 4—X-ray diffraction patterns of the simulated CGHAZs.

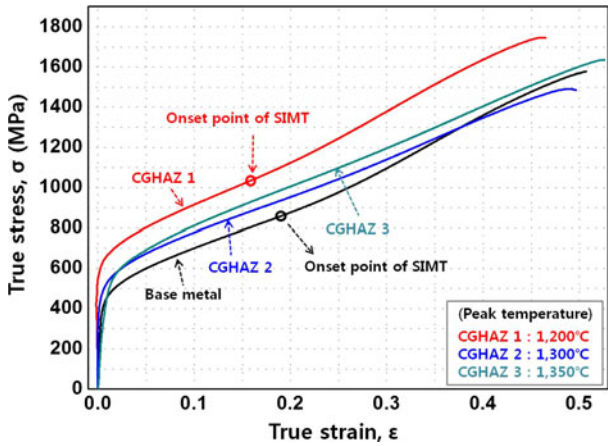

Fig. 5—True stress–true stain curves of the base steel and simulated CGHAZs.

was made through scanning electron microscope observation of hardness impression and microstructure. Note that, for a given geometrically self-similar sharp indenter (like a Berkovich indenter used in this study), the representative stress and strain underneath the indenter are unique and independent of indentation depth, which is different from a spherical indentation. Thus, if there is SIMT or DT, it should occur at the very early stage of loading and thus may not be easily detected in the curve for the relatively high peak load (*e.g.*, 10 mN here). In Figure 8, base steel shows the lowest displacement at the peak load, implying that the base steel has a higher hardness of austenite vis-à-vis the CGHAZs. It is interesting that the CGHAZs exhibit lower hardness than that of base steel because the former has higher amount of C and

N, which are effective elements for solid-solution hardening. This interesting result may be closely related to the competition between SIMT and DT in the samples. As mentioned above, the SIMT is pronounced in the base steel but disappeared with increasing δ-ferrite fraction in the CGHAZs. Therefore, although the base steel contained lower C and N contents in comparison with the weld CGHAZs, it had the highest nanohardness due to the formation of martensite during nanoindentation. Similarly, the lowest nanohardness of CGHAZ 2 and 3 may be explained by the absence of strain-induced martensite. The similar hardness value of CGHAZ 2 and 3 is in a good agreement with the fact that the samples had a similar δ-ferrite fraction despite different peak temperature (see Table I).

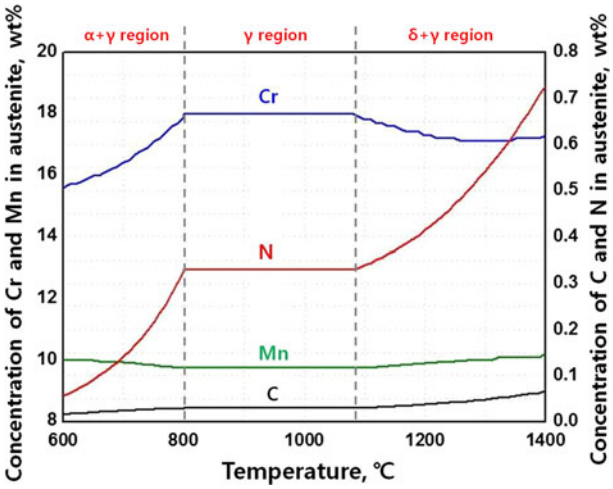

Fig. 6—Calculated solute concentration in austenite region with increasing temperature.

D. *Stacking Fault Energy*

In the literature,[6,14–19] it has been well accepted that deformation of austenite is greatly affected by its SFE. With increasing SFE, the deformation mechanism of austenite changes from SIMT to DT and dislocation slip gradually. Therefore, many research groups have concentrated their effort on measuring or calculating SFE,[5,20–23] and much previous research proposed the SFE value of the range of 20 to 30 mJ/m^2, as an upper transition point from SIDT to DT.[14–19] However, in previous works,[14–19] the effect of N addition on the SFE has not been treated, whereas the alloy used in this study includes high N (see Table I), which means previous results[14–19] may not be directly applicable to our alloy. In some literature, the empirical ways to calculate SFE are provided with considering N addition, and Pickering[24] and Chen *et al.*[5] estimated the SFE by Eqs. [2] and [3], respectively.

$$\text{SFE}\ (\text{mJ/m}^2) = -25.7 + 2 \cdot \text{Ni} + 410 \cdot \text{C-0.9} \cdot \text{Cr-77} \cdot \text{N-13} \cdot \text{Si-1.2} \cdot \text{Mn} \quad [1]$$

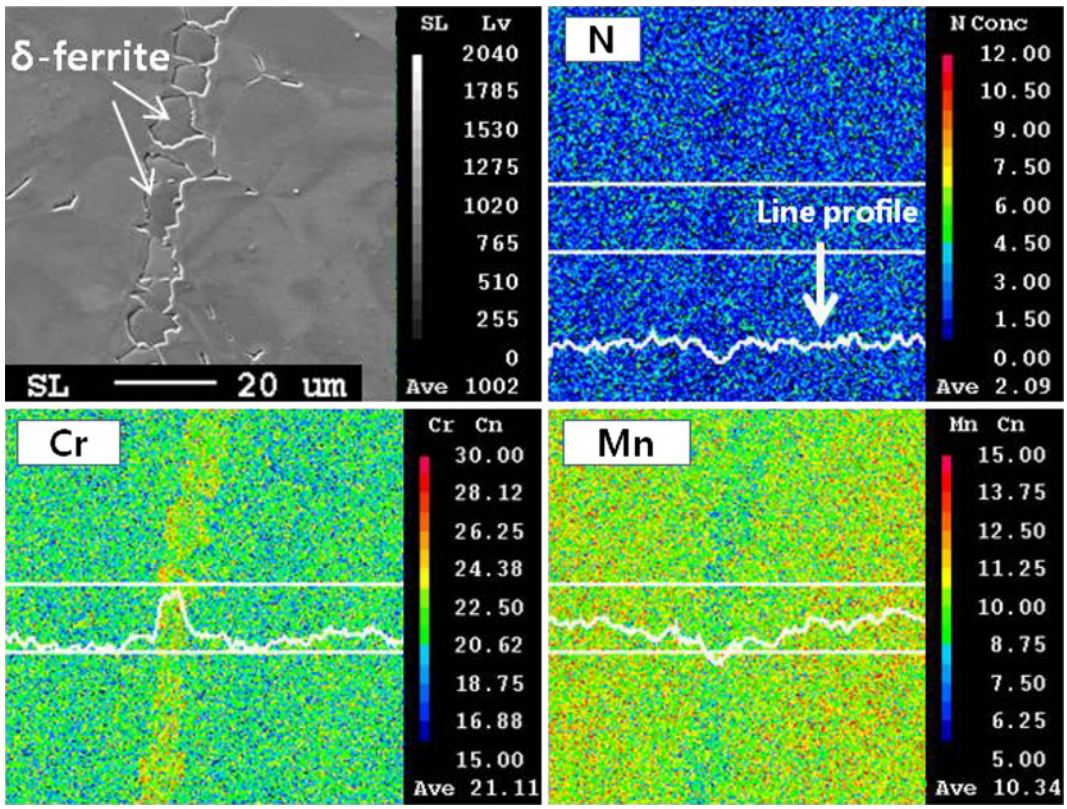

Fig. 7—EPMA results showing distribution of alloying elements in the weld CGHAZ.

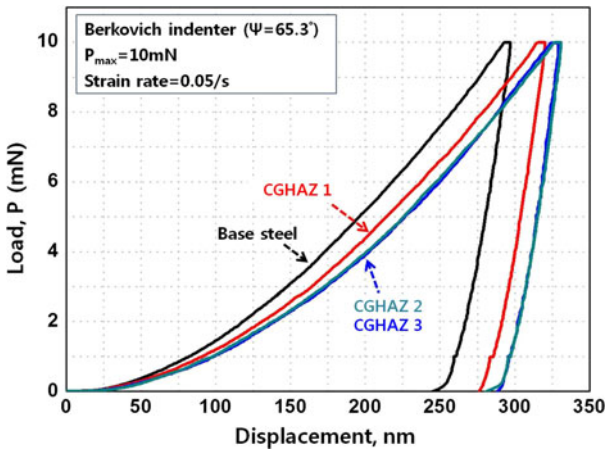

Fig. 8—Nanoindentation curves of the base steel and simulated CGHAZs.

$$\text{SFE}\ (\text{mJ/m}^2) = 34 + 1.4 \cdot \text{Ni} - 1.1 \cdot \text{Cr} - 77 \cdot \text{N} \quad [2]$$

The chemical compositions in Eqs. [1] and [2] are in wt pct. Both equations resulted in the negative SFE values of –67.4 mJ/m^2 and –11.2 mJ/m^2 for our base steel, and this discrepancy is presumably due to the difference in chemical composition, especially Ni; Eqs. [1] and [2] were established by linear fitting of experimentally measured SFE in high-Ni austenitic stainless steel.

Lee *et al.*[6] measured the SFE by the Rietveld whole profile fitting and the double-Voigt size-strain analysis for neutron diffraction profile of tensile-strained specimens of Fe-18Cr-10Mn-N-C alloys and reported that SFE of the austenite phase increased with increasing N + C contents, leading to changing the deformation mode from SIMT to DT. To verify this finding, they presented TEM micrographs showing ε martensite, α' martensite, and deformation twin in tensile-strained specimen depending on their C + N contents.

The composition of the examined alloy (Fe-17.96Cr-9.74Mn-0.03Si-0.33N-0.03C [wt pct]) in this study can be regarded as an extension of system treated by Lee *et al.*,[6] and thus the estimation of SFE of austenite in the base steel and CGHAZs can reasonably be made through a comparison with literature data. Lee *et al.* proposed a correlation between the SFE (depending on C + N atomic percent) and deformation microstructure. To calculate concentrations of C and N in the CGHAZs, this study assumes a local paraequilibrium condition. As shown in Figure 7, Cr is enriched in ferrite region, while Mn and N are enriched in austenite region. Figure 9 shows a schematic diagram showing profiles of alloying elements in the CGHAZs. In the figures, X^0_{Cr} and X^0_{Mn} are the initial solute concentrations of Cr and Mn in the base steel, $X^e_{\text{Cr in } \delta\text{–ferrite}}$, $X^e_{\text{Mn in } \delta\text{–ferrite}}$, and $X^e_{\text{C \& N in } \delta\text{–ferrite}}$ are the solute concentrations of Cr, Mn, C, and N in δ–ferrite of the CGHAZs and $X^e_{\text{Cr in } \gamma}$, $X^e_{\text{Mn in } \gamma}$, and $X^e_{\text{C\&N in } \gamma}$ are the solute concentrations of Cr, Mn, C, and N in austenite of the CGHAZs, respectively. As shown in Figure 9, a partitioning of alloying elements occurs depending on the δ-ferrite

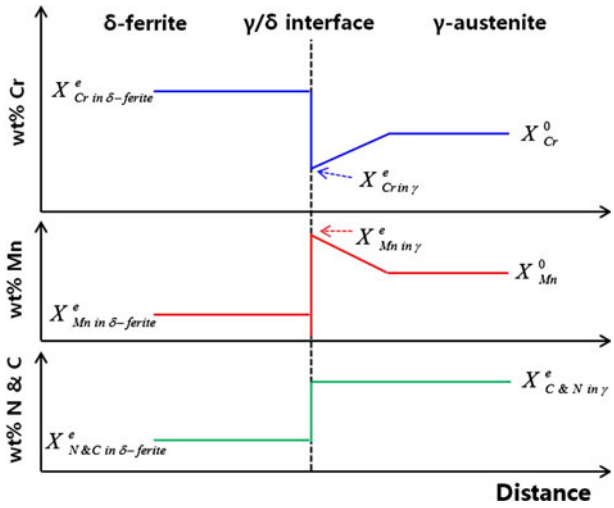

Fig. 9—Schematic diagram showing profiles of alloying elements in the CGHAZs.

formation, and Cr and Mn should be depleted and enriched at the γ/δ interface, respectively, while partitioning of N and C occurs according to equilibrium condition without depletion or enrichment at the γ/δ interface. This is closely related to the diffusivity of alloying elements. Note that the diffusion coefficient of interstitial elements, which are N and C in this study, was about four orders of magnitude greater than substitutional elements such as Cr, Ni, and Mn at a high temperature above 1073 K (800 °C).[25] As it is well known, a phase transformation from γ to δ-ferrite is a diffusion-controlled process, and thus, a local equilibrium at near γ/δ interface can be assumed as shown in Figure 9, *i.e.*, the solute concentration in γ adjacent to δ-ferrite will be reached to equilibrium values, while the solute concentration in γ away from δ-ferrite varied in each element. N and C could diffuse into γ immediately due to their high diffusivity despite the fast heating and cooling cycle in the CGHAZs and concentrated in γ according to equilibrium condition, while Cr and Mn in γ could not reach equilibrium condition due to their slow diffusion. It is noteworthy that the fraction of δ-ferrite in the CGHAZs does not reach an equilibrium value (see Table I), possibly leading to very little difference in the solute concentrations of C and N in γ phase from their equilibrium values described in Figure 9, which is not considered in the current study. With the concern for a partitioning of alloying elements, N and C contents in γ of CGHAZs were determined as equilibrium values (calculated using Thermo-Calc in Figure 6). To calculate the SFE of the tested alloys, this study makes the equation by linear fitting using the published data (data used for fitting are indicated as closed circles in Figure 10) in the previous work,[6] and Eq. [3] shows the fitted equation:

$$\text{SFE}\ (\text{mJ/m}^2) = 11 \cdot [\text{C} + \text{N}]\text{wt pct} - 6.8 \quad [3]$$

That is, this study calculated the SFE of the base steel and CGHAZs using Eq. [3] and the solute concentration of C and N in Figure 6. The estimated SFE of the base

steel and CGHAZs was in a reasonable agreement with literature data.[6] Figure 10 shows a correlation between SFE (depending on interstitial contents) and deformed microstructure. Previous work[6] reported that the change of deformation mode from SIMT to DT start over 2.0 at. pct C + N contents. Taking this into account, it can be expected in Figure 10 that the SIMT can occurs in base steel and the CGHAZ 1, while the SIMT is significantly retarded (and thus disappeared in the curves) in the CGHAZ 2 and 3 including over 2.0 at. pct C + N contents. The analysis in Figure 10 agreed well with the deformation behavior in Figure 5.

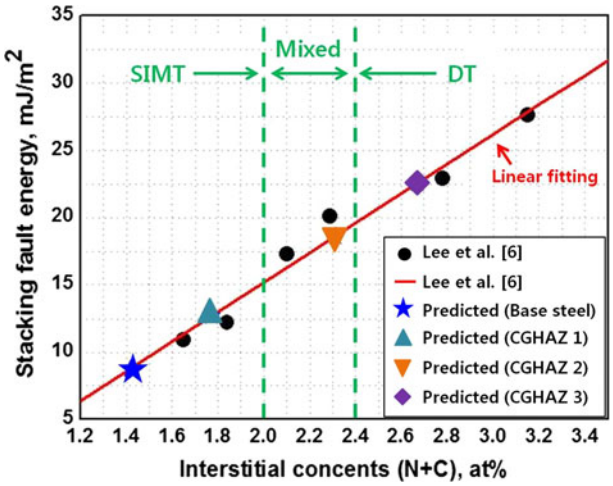

Fig. 10—Correlation between SFE and deformation microstructure of Fe-18Cr-10Mn-N alloy.[6]

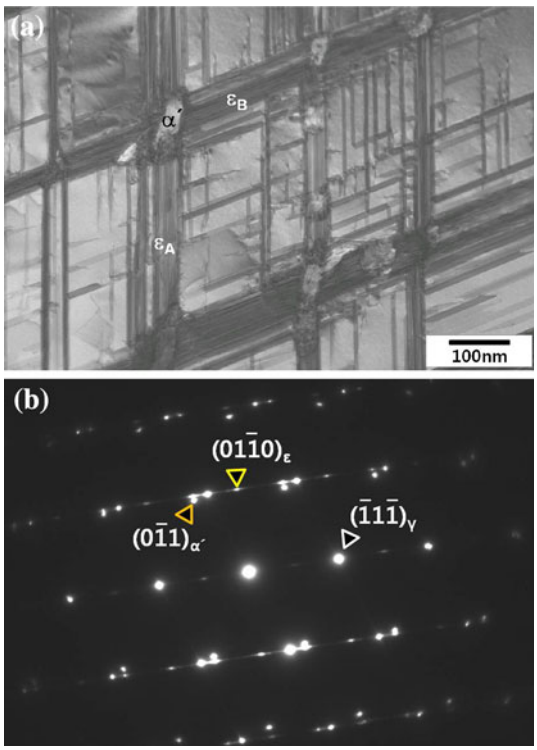

Fig. 11—TEM micrographs of base steel showing the formation of ε band, their interactions, and α' martensite after deformation: (*a*) BF image showing the formation of α' martensite at two ε intersection designated as ε_A, ε_B, and α' and (*b*) SAD pattern of $Z = [110]_\gamma$.

E. *Deformed Microstructure*

Figure 11(a) shows a scanning transmission electron microscopy bright-field image of the base steel after tensile deformation. It is obvious in the figure that the characteristic deformation bands consist of lots of overlapping bands of thin plates. In the selected-area diffraction (SAD) pattern of Figure 11(b), diffraction spots from the γ-austenite matrix are spread into streaks, and they can be indexed as ε martensite of hexagonal close-packed structure and α' martensite of body-centered cubic structure. The γ austenite has a Shoji-Nishiyama (S-N)[6] and Kurdjumov-Sachs (K-S)[26] orientation relationship with ε martensite and α' martensite, respectively, where the close-packed planes and directions of both structures are parallel.

$$[110]_\gamma // [\bar{2}110]_\varepsilon\,,\quad \{1\bar{1}1\}_\gamma // \{0001\}_\varepsilon \quad \text{(S-N relation)}$$

$$[110]_\gamma // [111]_{\alpha'}\,,\quad \{111\}_\gamma // \{110\}_{\alpha'} \quad \text{(K-S relation)}$$

Therefore, Figure 11 indicates that the γ-austenite of base steel was transformed to ε and α' martensite during tensile deformation, as discussed in the previous section.

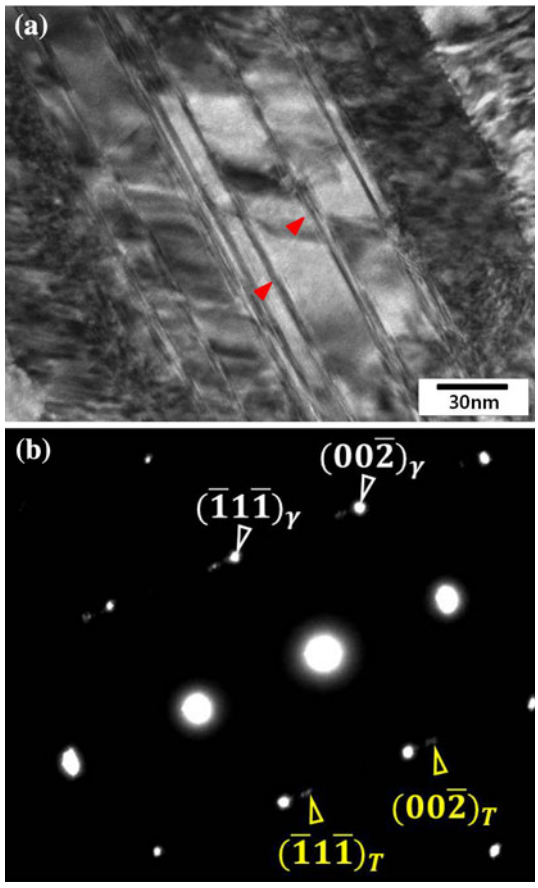

Fig. 12—TEM micrographs of CGHAZ 3 showing the deformation bands after deformation: (*a*) BF image of primary twin bands and (*b*) SAD pattern of $Z = [110]_\gamma$.

Meanwhile, the twin bands were found predominantly in the CGHAZ 3 after tensile deformation. Figures 12(a) and (b) show TEM micrograph and corresponding SAD pattern of deformation twinning taken from the CGHAZ 3. The deformation bands in Figure 12(a) consist of nanosized twins. This presence of DT can strongly support the idea that tensile deformation mode changed from SIMT to DT with increasing SFE of austenite depending on δ-ferrite formation in the CGHAZs. This change in deformation mode can explain the change of true stress–strain curves in Figure 5.

IV. CONCLUDING REMARKS

The influence of δ-ferrite formation on tensile deformation behavior in the CGHAZs of metastable austenitic Fe-18Cr-10Mn-N alloy was systematically investigated and discussed, and the following results were found:

1. During tensile test, the SIMT was clear in base steel but was disappeared and replaced by DT in CGHAZs. This is because the SFE in the CGHAZs increases with increasing peak temperature as C and N are concentrated in austenite phase. In the current work, DT occurred in CGHAZ 2 and 3, including over 2.0 at. pct C + N contents.
2. Interestingly, despite enrichment of alloying elements, the nanohardness of austenite in the CGHAZs was smaller than that of base steel, and this is due to SIMT in the base steel during tensile deformation.
3. TEM observation confirms the change in deformation microstructure according to δ-ferrite formation in the CGHAZs. The ε martensite bands and α' martensite providing evidence for SIMT were found in base steel, while DT bands were indentified in the CGHAZs.

ACKNOWLEDGMENTS

This research was supported by a grant from the Fundamental R&D Program for Core Technology of Materials funded by the Ministry of Knowledge Economy, Republic of Korea. The authors wish to thank Sang-Ho Han and Moo-Young Seok for their valuable support for the experimental works.

REFERENCES

1. I. Woo, T. Horinouchi, Y. Miyano, and Y. Kikuchi: *Steel Grips*, 2004, vol. 2, pp. 187–96.
2. T.H. Lee, C.S. Oh, and S.J. Kim: *Scripta Mater.*, 2008, vol. 58, pp. 110–13.
3. K.J. Irvine, D.T. Llewellyn, and F.B. Pickering: *J. Iron Steel Inst.*, 1961, vol. 199, pp. 153–75.
4. H.Y. Ha, T.H. Lee, C.S. Oh, and S.J. Kim: *Scripta Mater.*, 2009, vol. 61, pp. 121–24.
5. R.E. Schramm and R.P. Reed: *Metall. Trans. A*, 1975, vol. 6A, pp. 1345–51.
6. T.H. Lee, E. Shin, C.S. Oh, H.Y. Ha, and S.J. Kim: *Acta Mater.*, 2010, vol. 58, pp. 3173–86.
7. H.K.D.H. Bhadeshia: *ISIJ Int.*, 2002, vol. 42, pp. 1059–60.
8. K. Sugimoto, M. Kobayashi, and S. Hashimoto: *Metall. Trans. A*, 1992, vol. 23A, pp. 3085–91.
9. Y. Miyano, H. Fujii, Y. Sun, Y. Katada, S. Kuroda, and O. Kamiya: *Mater. Sci. Eng. A*, 2011, vol. 528, pp. 2917–21.
10. K. Easterling: *Introduction to the Physical Metallurgy of Welding*, Butterworth, London, U.K., 1983, pp. 17–26.
11. T.H. Lee, S.J. Kim, and S. Takaki: *Metall. Mater. Trans. A*, 2006, vol. 37A, pp. 3445–54.
12. J.W. Simmons: *Acta Mater.*, 1997, vol. 45, pp. 2467–75.
13. J. Moon, S. Kim, J.I. Jang, J. Lee, and C. Lee: *Mater. Sci. Eng. A*, 2008, vol. 487, pp. 552–57.
14. L. Remy and A. Pineau: *Mater. Sci. Eng. A*, 1976, vol. 26, pp. 123–32.
15. Y.K. Lee and C.S. Choi: *Metall. Mater. Trans. A*, 2000, vol. 31A, pp. 355–60.
16. G.B. Olson and M. Cohen: *Metall. Trans. A*, 1976, vol. 7A, pp. 1897–1904.
17. I. Karaman, H. Sehitoglu, and Y.I. Chumlyakov: *JOM*, 2002, vol. 7, pp. 31–37.
18. S. Cruze and V.T. Kuokkala: *Acta Mater.*, 2010, vol. 58, pp. 5129–41.
19. S. Allain, J.P. Chateau, O. Bouaziz, S. Migot, and N. Guelton: *Mater. Sci. Eng. A*, 2004, vols. 387–389, pp. 158–62.
20. C.G. Rhodes and A.W. Thompson: *Metall. Trans. A*, 1977, vol. 8A, pp. 1901–06.
21. A. Saeed-Akbari, J. Imlau, U. Prahl, and W. Bleck: *Metall. Mater. Trans. A*, 2009, vol. 40A, pp. 3076–90.
22. K. Sato, M. Ichinose, Y. Hirotsu, and Y. Inoue: *ISIJ Int.*, 1989, vol. 29 (10), pp. 868–77.
23. S. Cruze, V.T. Kuokkala, A. Oikari, J. Tolenen, and H. Hänninen: *Acta Mater.*, 2011, vol. 59, pp. 1068–76.
24. F.B. Pickering: *Proc. Stainless Steels*, The Institute of Metals, London, U.K., 2007, pp. 2010.
25. L. Chen, H. Tan, Z. Wang, J. Li, and Y. Jiang: *Corros. Sci.*, 2012, vol. 58, pp. 168–74.
26. D.A. Poter and K.E. Easterling: *Phase Transformation in Metals and Alloys*, 2nd ed., Chapman & Hall, London, U.K., 1992, p. 148.